

# Tactile sensing-processing: Interface-cover geometry and the inverse-elastic problem

Gábor Vásárhelyi<sup>a,\*</sup>, Balázs Fodor<sup>b</sup>, Tamás Roska<sup>c</sup>

<sup>a</sup> Péter Pázmány Catholic University, Department of Information Technology, Práter utca 50/a, H-1083 Budapest, Hungary

<sup>b</sup> Budapest University of Technology and Economics, Department of Machine Design, Műegyetem rakpart 3-9, H-1111 Budapest, Hungary

<sup>c</sup> Computer and Automation Research Institute of the Hungarian Academy of Sciences (MTA SZTAKI), Kende u. 13, H-1111 Budapest, Hungary

Received 15 September 2006; received in revised form 11 April 2007; accepted 27 May 2007

Available online 2 June 2007

## Abstract

The skin-like elastic cover of a tactile-sensor array plays a fundamental role in determining how the sensor is responding to an arbitrary surface stimulus. Indeed, this cover is the first spatial–temporal sensory instruction in a tactile cellular wave-computer, or in living, neural-tactile signal-processing organs. While the sensor under the elastic layer measures the local strain/stress, we are interested in the stimulating force distribution at the contacting surface. This paper deals with the described inverse problem in the stationary case over a three-axial tactile-sensor array, measuring three components of the local strain tensor of the elastic cover. Our goal here is to *design* an interface flexible cover to enhance specific capabilities, sensitivity and accuracy, when using the three-axial sensor array. First, on the simplest, *flat* rubber surface, we create a kind of tactile hyper-accuracy by giving a simple analytical solution to the case when the cover is indented by an arbitrary point load. Second, instead of generalizing our solution to more complex indentation profiles, we try to abolish the need for the complex inverse solution by specifying our cover's geometry and thus reducing the complexity of the sensor's coding mechanism. We create *hemispherical bumps* over the elastic surface and use a finite-element model to show that with the bumps we can localize the (otherwise continuous) input over the taxels and detect normal and shear force components independently. Finally, we confirm our theoretical results with real-time experimental data and use the measurements for sensor calibration and texture classification.

© 2007 Elsevier B.V. All rights reserved.

**Keywords:** Inverse-elastic problem; Tactile hyper-accuracy; Elastic hemispheres; Tactile-texture classification

## 1. Introduction

It has been known that the flexible cover plays an important role in tactile sensing, in biological and in artificial cases alike. In that framework, the inverse problem of the elastic cover on top of a tactile-sensor has been attracting the attention of scientific groups for decades now, but it still remains an interesting and difficult task to deal with. The rubber-like material – even if treated as homogeneous and isotropic – entails a quite complex behavior. Therefore, even the direct problem (i.e. when we know the force distribution on the contacting surface, and we want to find out the stress/strain distribution deep inside the rubber) needs special care and thus can be solved analytically only in restricted cases.

The direct-elastic problem of tactile-sensors was first mentioned by Ref. [1] for describing the stress distribution in the human skin, using the elastic half-space model; a more detailed, general contact analysis is found in Ref. [2]. The inverse problem was treated by many groups, but most of them had sensors measuring solely the normal stress/strain component; therefore, they constructed incomplete methods using scarce information. For the static case of a point load Fearing and Hollerbach [3] described an analytical but not practical and not completely solved method. The same group used linear [4] and nonlinear [5] inverse-filter processes to determine the curvature and location of objects, but their methods are far from real-time. They also work in a different spatial domain—their characteristic sizes are about one order of magnitude larger than ours. Numerical solutions using neural network training to determine object shapes can be found in Ref. [6], however, reliable experimental data are not provided. Chen et al. [7] investigates the inverse problem using moments and iterative algorithms, but

\* Corresponding author.

E-mail address: [vasarhelyi@itk.ppke.hu](mailto:vasarhelyi@itk.ppke.hu) (G. Vásárhelyi).

they need to combine signals from more than one sensor at once, and lack good experimental data again. Many other groups were trying to extract different features from tactile data, but all of them missed to have a reliable and small enough tactile-sensor, measuring at least three components of the strain/stress tensor. Having developed these sensors, we can first concentrate on the basic solutions again.

In the first part of the paper we investigate what we can extract from measurements on *one single taxel* and a *flat cover*. We derive an analytical inverse-solution for a point load, perpendicular to the surface; namely, we determine the exact location and the amplitude of the normal load by measuring three local strain components at one point under the cover, thereby creating a kind of tactile hyper-accuracy. We support our results with real-time experimental data, and also extend the analytical solution to a three-component point load, using more than one taxel.

Since the inverse solution can be solved only in this very restricted case, in the second part we investigate how changes in the surface geometry could be used to extend the information provided via the elastic layer. The idea that the geometry of an elastic cover should be used to enhance tactile signals is well known from nature. Fingerprints are present on our fingers to increase the sensitivity of the tactile receptors that lie under them. During tactile manipulation the first contact points on the skin will be the emerging parts, with the highest stress values around them. Bolanowski and Pawson [8] show that the Meissner receptors of monkeys lie mostly along the ridges of fingerprints. Fingerprints also modify the stress/strain distribution inside the skin, which can be beneficial for the tactile system. Fearing and Hollerbach [3] mention the stress enhancing effect of the papillary ridges first, and calculate the locations with maximal stress for a sinusoidal surface. Gerling and Thomas [9] investigate the “lensing effect” of the fingerprints, i.e. the edge enhancing behavior of the ridges. Maeno et al. give a detailed description on where the tactile receptors are located, and why—also including the role of ridged surfaces [10]. They also create a huge artificial finger skin with ridges [11] and use it to extract some shear information from the underlying sensors to prevent slippage during grasping tasks. Instead of the direction selective ridges, simple elastic hemispheres could also be used: Tremblay and Cutkosky [12] describe in detail how hemispheres on the elastic cover enhance gripping properties of a sensor. They use these bumps to transfer vibrations to accelerometers when released by the grip.

Here, we follow a different strategy: our goal is to design a cover geometry that enhances the capability and sensitivity of the entire tactile system. To achieve this, we also use hemispheres on the elastic surface. We give a detailed finite-element analysis on the behavior of the elastic bumps in different loading situations, and show that they provide a chance to avoid the solution of the inverse problem of the cover. With measurements on the proper cover – designed according to the finite-element model – we confirm that the bumps can be used efficiently to localize the load over the taxels and code the three local indentation components independently. Finally, we use our new sensor design for tactile-texture classification, too.

In Section 2 we give an introduction to the three-axial sensor design used in our work. The solution to the inverse problem of the flat cover can be found in Section 3 with detailed mathematics, while Section 4 shows our experimental results concerning the deduced tactile hyper-accuracy model. Section 5 introduces the finite-element model describing the behavior of the elastic bumps on the cover surface, while Section 6 gives experimental results for this cover type, with a texture-classification example. Conclusions and acknowledgments can be found afterwards.

## 2. Sensor design

Since our results are fundamentally connected to our tactile arrays, we start our analysis with a short description of the sensor design in question. Our MEMS array is developed at the Research Institute for Technical Physics and Materials Science (MFA) of the Hungarian Academy of Sciences. Detailed description of the sensor can be found in Refs. [13,14]. The piezoresistive  $2 \times 2$  array is made from monocrystalline silicon by porous Si micromachining. Every taxel in the array consists of four piezoresistors, each embedded into one of the suspension bridges, having its reference pair on the surrounding rigid substrate (Fig. 1). The three components of the load applied to the bridge can be calculated from the four signals of the piezoresistors. If the sensor is covered by an elastic layer, these components become linear functions of three elements of the local strain tensor of the cover at the center of the bridges, at a depth of the cover thickness.

With the protective elastic cover we invest the point-like sensor with a receptive field of a certain finite size, and, therefore, we create a structure with spatially continuous input and discrete output. Our goal is thus to decode this continuous input from the discrete measurements. Obviously, this inverse problem is not an easy task; hence, we restrict ourselves first to the most basic case—a stationary point load.

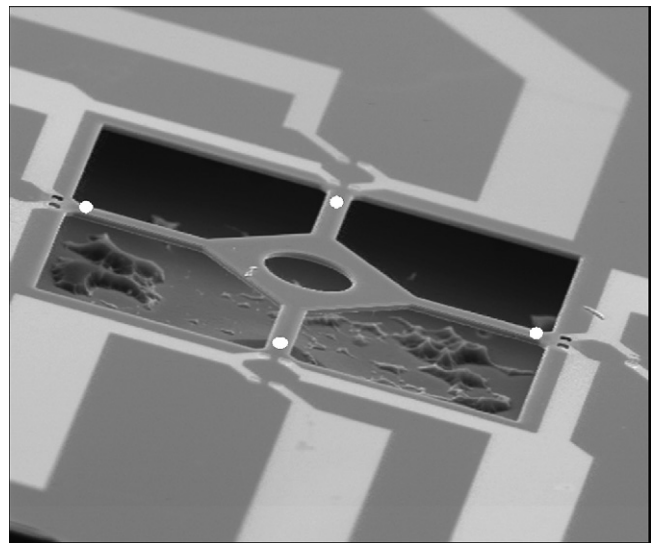


Fig. 1. SEM view of one taxel of the MEMS array without the elastic cover. The location of the piezoresistors is illustrated with four white circles. The width of the sensor is 300  $\mu\text{m}$ .

### 3. Inverse solution for a point load

The frame of reference is the elastic half-space [2], with homogeneous and isotropic behavior in the stationary case. The axes  $x$  and  $y$  are taken along the rubber surface, while  $z$  points into the half-space. The point load at  $(0, 0, 0)$  can be described with its three components  $Q$ ,  $R$  and  $F$ , while the three measured strain-tensor components at the sensor location  $(x, y, z)$  are  $u_{xz}$ ,  $u_{yz}$  and  $u_{zz}$  (Fig. 2). Note that the real cover with finite thickness is approximated here with infinite size, and strain values are taken at the given finite depth of the sensor. This simplification, however, does not affect the results much, because inside the material stress/strain decays rapidly with space.

Our solution of the equilibrium equation in the elastic half-space – i.e. the strain distribution caused by an arbitrary point load – can be found in Ref. [2]. As a useful, but not harmful simplification, in the final equations we set the Poisson's ratio to 0.5. Hence, the solution takes the following form (with  $E$  denoting the Young modulus):

$$\begin{pmatrix} u_{xz} \\ u_{yz} \\ u_{zz} \end{pmatrix} = \frac{3(Qx + Ry + Fz)}{4\pi E(x^2 + y^2 + z^2)^{5/2}} \begin{pmatrix} -3xz \\ -3yz \\ x^2 + y^2 - 2z^2 \end{pmatrix}. \quad (1)$$

Our goal is now to express  $Q$ ,  $R$ ,  $F$ ,  $x$  and  $y$  with the three strain components. We introduce polar variables  $\alpha$  and  $\rho$  on the surface, where  $\alpha$  can be derived simply from the strain components:

$$\tan \alpha = \frac{y}{x} = \frac{u_{yz}}{u_{xz}}, \quad \rho^2 = x^2 + y^2. \quad (2)$$

We also introduce a dimensionless variable  $A$ , which can be calculated from the three measured strain components, too:

$$A^2 = \frac{u_{xz}^2 + u_{yz}^2}{u_{zz}^2} = \frac{9z^2\rho^2}{(\rho^2 - 2z^2)^2}. \quad (3)$$

Since  $A$  is a measured value and  $z$  is known from the sensor design, (3) becomes a simple second-order equation for  $\rho^2$ , with the two solutions:

$$\rho_{1,2}^2 = z^2 \left( 2 + \frac{9 \pm \sqrt{81 + 72A^2}}{2A^2} \right). \quad (4)$$

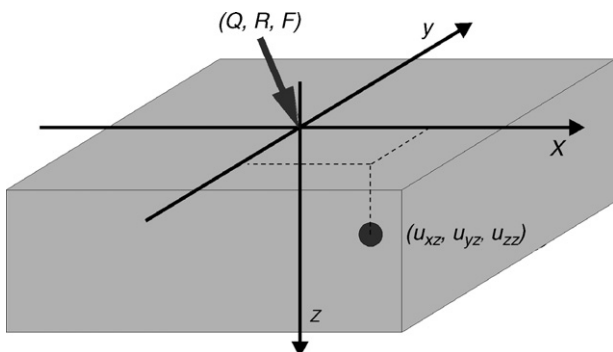


Fig. 2. Schematic view of the point load on the surface of the elastic half-space, and the sensor inside the material.

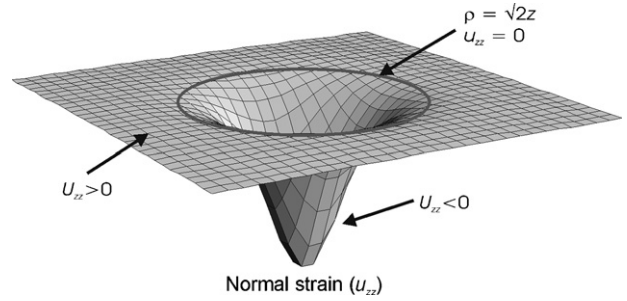


Fig. 3. Strain distribution ( $u_{zz}$ ) under a normal point load. The main region of interest – within a radius of  $\sqrt{2}z$  around the load – is when the normal strain takes negative values. In this case the inverse method can be based on reliable experimental data with high SNR.

#### 3.1. Partial solution for a normal load

From now on we take  $Q = R = 0$  for a while (i.e. only the normal load component is present), in order to analyze the solution more precisely. In that case three distinct regions for  $\rho$  can be separated depending on the  $u_{zz}$  distribution (Fig. 3).

When  $\rho < \sqrt{2}z$ , the normal strain component ( $u_{zz}$ ) becomes negative—basically this is the region where  $u_{zz}$  is accurately measurable. In this case for  $\rho^2$  we get the value:

$$\rho^2 = z^2 \left( 2 - \frac{12}{\sqrt{9 + 8A^2} + 3} \right). \quad (5)$$

If  $\rho = \sqrt{2}z$ ,  $u_{zz}$  becomes zero and  $A$  goes to infinity. With  $\rho > \sqrt{2}z$ ,  $u_{zz}$  becomes positive, and we get:

$$\rho^2 = z^2 \left( 2 + \frac{12}{\sqrt{9 + 8A^2} - 3} \right). \quad (6)$$

It is exciting to see that with the thickness of the rubber we can adjust the radius of the region where  $u_{zz}$  is negative and where the properties of the force can be recovered with high precision. However, by thickening the rubber, we need higher force values to give high enough strain in the rubber for the measurement.

After determining  $\rho$  and  $\alpha$ , we can calculate  $x$  and  $y$  easily:

$$x = \rho \cos \alpha, \quad y = \rho \sin \alpha. \quad (7)$$

The amplitude of the force is extracted from any component of (1) now (e.g. from  $u_{zz}$ ):

$$F = u_{zz} \frac{4\pi E(\rho^2 + z^2)^{5/2}}{3(\rho^2 - 2z^2)z}. \quad (8)$$

From one point of measurement these are all the data we can reconstruct analytically. If the loading force has more than one component, (8) takes the following form:

$$Qx + Ry + Fz = u_{zz} \frac{4\pi E(\rho^2 + z^2)^{5/2}}{3(\rho^2 - 2z^2)}. \quad (9)$$

In this case we need more restricting assumptions for determining the force components. For example, if we know the friction coefficient ( $\mu$ ),  $Q$  and  $R$  can be expressed with  $F$ , and hence the normal and tangential components can be separated.

Note that if we had sensors measuring the *stress* in the material, and not the *strain*, the equations would become even simpler, and we would avoid the singularity at  $\rho = \sqrt{2}z$ . Substituting strain for stress in the definition of  $A$  and  $\alpha$ , instead of (1) and (4) now we write:

$$\begin{pmatrix} \sigma_{xz} \\ \sigma_{yz} \\ \sigma_{zz} \end{pmatrix} = \frac{3(Qx + Ry + Fz)}{2\pi(x^2 + y^2 + z^2)^{5/2}} \begin{pmatrix} -xz \\ -yz \\ -z^2 \end{pmatrix}. \quad (10)$$

and

$$\rho = zA\sigma. \quad (11)$$

### 3.2. Full solution using a sensor array

Having a rectangular array of strain sensors at a depth of  $z$ , with a given  $d$  distance between the neighboring sensors, we need to fulfill the following constraint to have at least three sensors close enough to the point load at all times:

$$d < \frac{1 + \sqrt{2}}{2}z \approx 1.2z. \quad (12)$$

This has not yet been achieved in our sensor-array design; hence this section so far remains a theoretical assumption. With three sensors we have three equations similar to (9). We calculate their right side and name it  $M$ :

$$Qx_i + Ry_i + Fz = u_{zzi} \frac{4\pi E(\rho_i^2 + z^2)^{5/2}}{3(\rho_i^2 - 2z^2)} = M_i \quad (i = 1, 2, 3). \quad (13)$$

From this the general solution can be deduced using simple algebraic calculations:

$$\begin{aligned} Q &= \frac{(M_2 - M_3)y_1 + (M_3 - M_1)y_2 + (M_1 - M_2)y_3}{(x_2 - x_3)y_1 + (x_3 - x_1)y_2 + (x_1 - x_2)y_3}, \\ R &= \frac{(M_2 - M_3)x_1 + (M_3 - M_1)x_2 + (M_1 - M_2)x_3}{(x_3 - x_2)y_1 + (x_1 - x_3)y_2 + (x_2 - x_1)y_3}, \\ F &= \frac{(M_3x_2 - M_2x_3)y_1 + (M_1x_3 - M_3x_1)y_2 + (M_2x_1 - M_1x_2)y_3}{[(y_2 - y_1)x_3 + (y_1 - y_3)x_2 + (y_3 - y_2)x_1]z}. \end{aligned} \quad (14)$$

### 3.3. Considerations with real sensors

When checking the validity of our theory on real sensors, we need to take into account that their signals are not the exact strain tensor components but their linear functions with different slope in the normal and shear directions. The characterizing equation of a single taxel is as follows:

$$\begin{pmatrix} u_{xz} \\ u_{yz} \\ u_{zz} \end{pmatrix} = \begin{pmatrix} \alpha_s \\ \alpha_s \\ \alpha_n \end{pmatrix} \circ \begin{pmatrix} T_x \\ T_y \\ S_n \end{pmatrix}, \quad (15)$$

where  $T_x$ ,  $T_y$  and  $S_n$  are the three strain-like vector components calculated from the original voltage measurements,  $\alpha_n$  and  $\alpha_s$  are the *normal* and *shear* linear coefficients, connecting the real and

the measured strain tensor elements. The value of  $\alpha_n$  and  $\alpha_s$  is not calculated theoretically, but Refs. [13,14] proves their linear behavior, and now we provide a simple method for determining their relative values experimentally.

Calculating with (15) we need to change the definition of  $A$  slightly. Let us define  $A_m$  (from  $A_{\text{measured}}$ ) in the following way:

$$A_m^2 = \frac{T_x^2 + T_y^2}{S_n^2} = \left(\frac{\alpha_n}{\alpha_s}\right)^2 A^2 = \frac{1}{\beta_{ns}^2} A^2, \quad (16)$$

where we also define  $\beta_{ns}$  as the *normal-to-shear sensitivity* of the sensor. Substituting (16) into (5) we get:

$$\rho^2 = z^2 \left( 2 - \frac{12}{\sqrt{9 + 8(\beta_{ns}A_m)^2 + 3}} \right). \quad (17)$$

The value of  $\beta_{ns}$  is obviously not one. It depends on the sensor design and the adhesive properties of the elastic cover. However, it can be evaluated from a series of measurements—based on the following calculation. Let us take a look at (1) again, along the line  $y=0$ . Here  $u_{zz}$  has a minimum at  $x=0$ , while  $u_{xz}$  has an extremum at  $x = \pm z/2$ . From these extrema we get:

$$\left| \frac{u_{zz}|_{x=0;y=0}}{u_{xz}|_{x=\pm z/2;y=0}} \right| = \frac{1}{\beta_{ns}} \frac{|S_n|_{\max}}{|T_x|_{\max}} = \frac{25\sqrt{5}}{24}. \quad (18)$$

Now, if we move a point load along  $y=0$  on the real sensor, and save the three strain components in time (see Fig. 5 in the next section), from the measured distribution we can calculate how much the ratio of the maximal values differ from (18). That will be the  $\beta_{ns}$  ratio.

## 4. Measuring tactile hyper-accuracy with a flat cover

In the following we validate the theory of the previous section with measurements on the real three-axial sensors. In addition to showing the feasibility of our model, we measure the rate of tactile hyper-accuracy, achieved by utilizing only the flat cover and its previously introduced mathematical description. We also investigate the boundaries of our theory by giving a list of the possible sources of error.

For validating the previous section we constructed an experimental setup with the following parts (Fig. 4): (1) a measurement table that can be tilted, and moved subtly in two directions; (2) a high-precision stepper motor installed on the table, functioning in one dimension (1 mm = 320 steps, with further micro-stepper circuitry); (3) a loading needle that has a built-in strain-gauge, measuring the total loading force (needle diameter is 100  $\mu\text{m}$ , which is a good approximation of a point load); (4) a PC with specific evaluation software; (5) the MEMS array, covered with a 200  $\mu\text{m}$  thick silicon rubber<sup>1</sup> layer, with a Young modulus of approximately 2.4 MPa, calculated from its Shore A hardness of 45.

For proving the feasibility of our theory and for determining the normal and shear coefficients of the sensor, we

<sup>1</sup> Elastosil® RT-601.

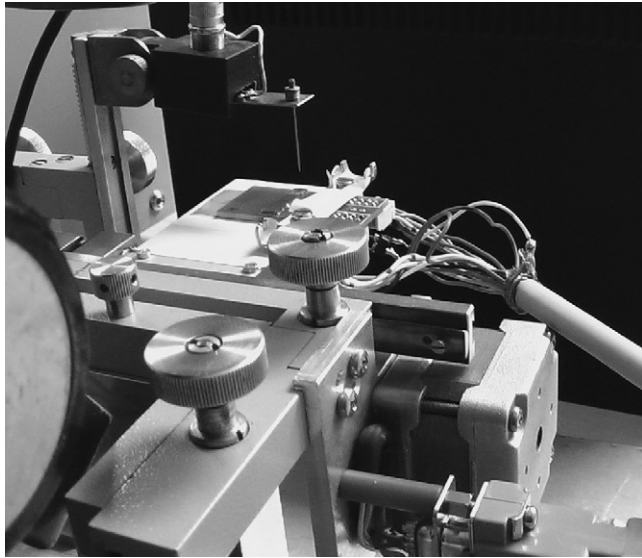


Fig. 4. The experimental setup with the measurement table, the stepper motor, the loading needle and the MEMS sensor.

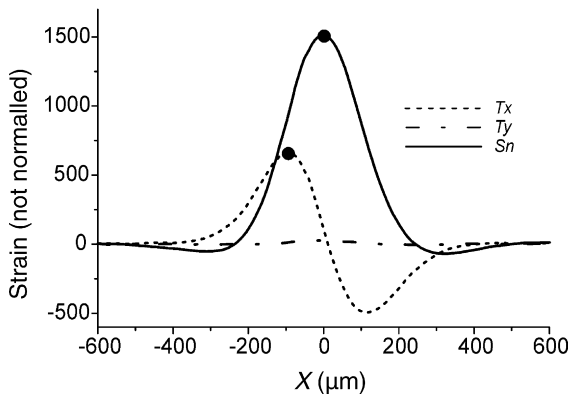


Fig. 5. The three measured strain components along the centerline ( $y=0$ ). The normal-to-shear ratio can be calculated from the ratio of the maximum values (signed with circles). The inverse equations are also based on this strain distribution.

carried out the following basic measurement: we applied a constant normal load on the rubber (approx. 20 mN), and used the stepper motor to move the needle slowly (0.5 mm/s) along the surface of the sensor in parallel

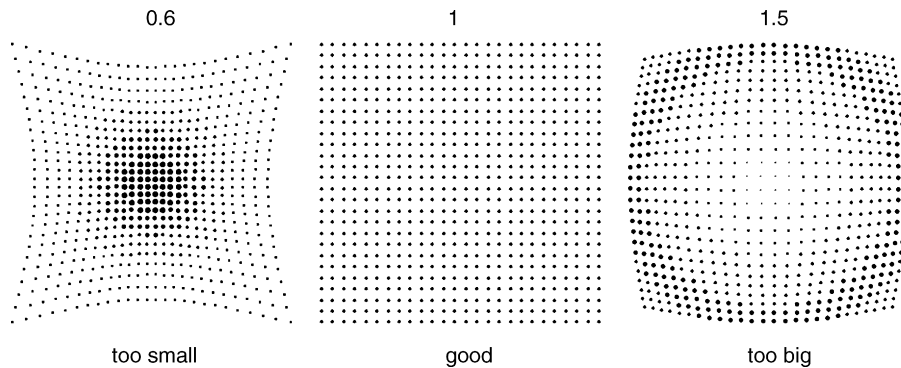


Fig. 6. Modeled results of the 2D point-load location-reconstruction experiment on a rectangular grid of points. The numbers above each plot represent the value of the normal-to-shear ratio chosen for the location and amplitude reconstruction. Amplitude is represented by the size of each point. Altering the normal-to-shear ratio changes the homogeneous mapping of the calculated locations and load amplitudes.

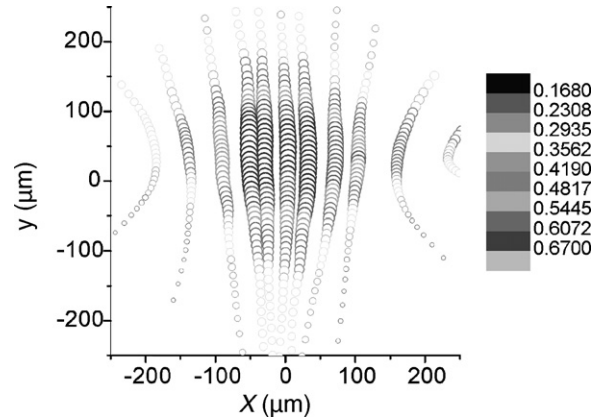


Fig. 7. Location and amplitude reconstruction of a point load, moved by a stepper motor over one taxel along parallel lines. Each circle is one data-acquisition point, measured by our software at 30 Hz. The two axes show the plane of the reconstructed surface coordinates, while both the size and color of the circles represent the local reconstructed load amplitude.

lines over the whole receptive field of the sensor. In the meantime we recorded the output of the sensor at about 50 fps.

With (18) and the previously described measurement we can calculate  $\beta_{ns}$  easily from the measurement along the line  $y=0$  (Fig. 5). After six measurements on the same taxel we got  $\beta_{ns} = 1.46 \pm 0.04$ , which means that the sensor is more sensitive to normal forces than to shear ones. This is what we would expect taking a look at the flat sensor design. Note that there exist several methods aiming to enhance the shear-strain transmission [14,15]. It can be done by changing the sensor design, at the price of losing the described analytical characteristics, as we will show in detail later.

As a next result, we transformed the measured data on the whole plane into coordinates and force amplitude using the deduced inverse equations and the determined value for  $\beta_{ns}$ . To see the pure effects of the changes in  $\beta_{ns}$  we modeled the results first on a rectangular grid of points with errorless theoretical data (Fig. 6).

Similar results can be seen in Fig. 7 reconstructed from the measurement data, using  $\beta_{ns} = 1.5$ , as an approximately feasible value.

The experimental result in Fig. 7 shows that our model is fully functional. There is quite a bit of error far from the center of the taxel, and the mapping of the reconstructed locations there resembles the underestimation of  $\beta_{ns}$ . In other words, the deviation between the measured strain distributions and the model is not constant; it is a function of distance from the center of the taxel. This function is not known theoretically, but aiming at better results it can be measured point by point as calibration data. Nevertheless, within a radius of approximately 150  $\mu\text{m}$  this is not needed, because reconstructed locations and amplitudes are reliably calculated there. Here we achieve kind of a tactile hyper-accuracy with an approximate precision of 3–5  $\mu\text{m}$ .

The absolute value for the normal and shear coefficients can be determined by comparing the known load amplitude and the calculated one. However, the feedback from our current strain gauge in the loading needle is not reliable enough for precise calibration.

Knowing the exact speed of the stepper motor and the data acquisition rate, we were also able to give quantitative results. We took the measurement points that correspond to the middle line of Fig. 7, and measured its slope in time (Fig. 8).

The calculated speed (0.45 mm/s) is a bit less than the real value (0.5 mm/s), but it can be compensated with a linear constant again, which is kind of the same as raising the cover thickness a bit in the model.

#### 4.1. Error estimation

This section is only a qualitative enumeration of the facts that have a possible effect on the results. There are quite a lot of things that could be taken into account. Here we only present the most significant ones. According to our knowledge, the sources of error could be the following:

- Our model is infinite, with homogeneous and isotropic behavior and with a Poisson's ratio of 0.5. The real sensor design is finite, with some nonlinearity at high strain values. Since modifying the model is quite a bit of a challenge, we take this source of error as a fact, and treat the results accordingly.
- The point load is a needle with finite diameter. However, the tip of the needle was treated to be hemispheric to cause

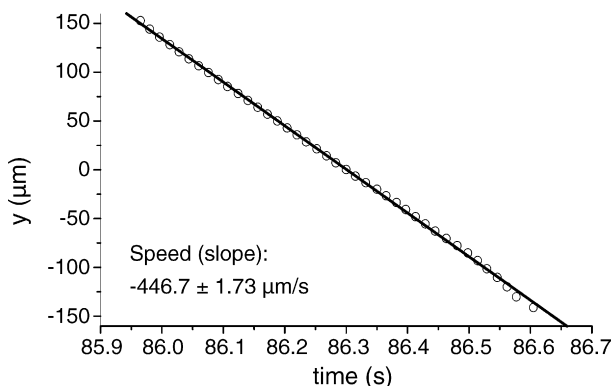


Fig. 8. Stepper motor speed calibration on the reconstructed locations along the center measurement line ( $y = 0$ ).

similar strain distribution to the point load (the similarity is getting more profound anyway with increasing distance in the material away from the indentation point).

- The sensor itself also has finite size. Details about this point can be found in Ref. [14].
- The experimental testing is very delicate, because the loaded sensor is quite sensitive to mechanical vibrations. A few microns of dislocation in the loading needle causes huge changes in the loading force and, therefore, in the measured strain values, too. The deviation of the rubber surface from a perfect plane, hence, causes the same effect.
- The stepper motor's magnetic field sometimes creates high frequency noise in the measured data.

### 5. Finite-element model of the elastic hemisphere

In the previous sections we saw how the location and the amplitude of a point load can be reconstructed analytically using the elastic half-space model. However, if the indentation is more complex (as in any general tactile manipulation task) and its spatial resolution is below the receptive field size of the taxels, this inverse problem becomes enormously difficult to solve.

Some basic issues on what we can do in this case can be found in Ref. [14]. One possible solution to this problem is the discretization of the continuous input by minimizing the receptive field, which can be done by *elastic hemispheres* on the cover surface. With these bumps we step over the boundaries of the elastic half-space model. Therefore, in this section we create a finite-element model of an elastic hemisphere, and describe the behavior of our newly shaped cover under different indentations.

Our model is an extension of the well-described elastic half-space, with a hemispherical bump on its surface. In the model we calculate with infinite size once again, and take strain/stress/deformation values from a given depth, at the point where the sensors are to be located. The elastic material is assumed to be homogeneous and isotropic, with a Young modulus of 0.87 MPa and Poisson's ratio of 0.499. The value of the Young modulus is only a linear constant in the equations and

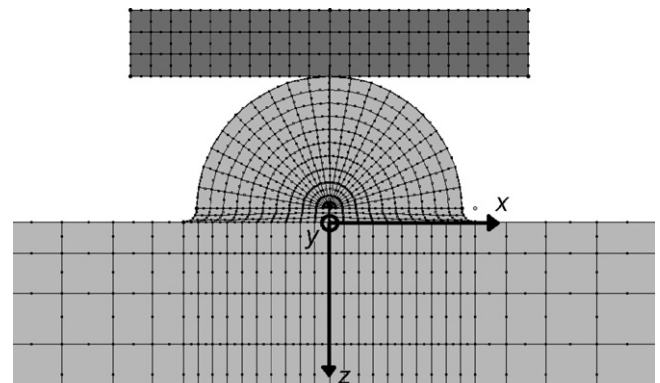


Fig. 9. The finite-element model of the bump over the elastic half-space. The flat and rigid indentation touches the top of the hemisphere.

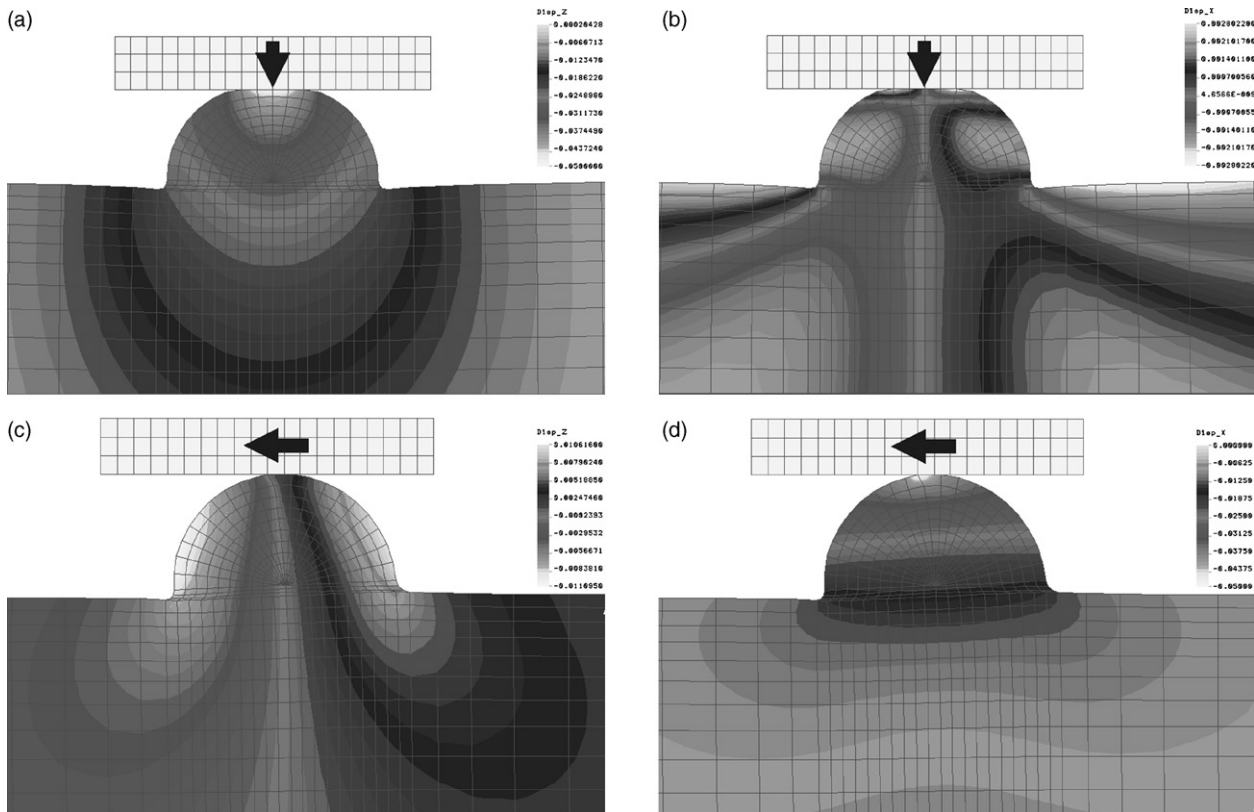


Fig. 10. Deformation caused by different loads. Components: (a) load:  $z$ , deformation:  $z$ ; (b) load:  $z$ , deformation:  $x$ ; (c) load:  $x$ , deformation:  $z$ ; (d) load:  $x$ , deformation:  $x$ .

smaller values for the Poisson's ratio do not change the FE results substantially either. We used the Cosmos Geostar 2.8 (128K version) FE package, with a total number of 1060 elements in the structure (Fig. 9).

In the first run the structure was only two-dimensional, with plain-stress approximation along the infinite third dimension (perpendicularly to the plane of this paper). This infinite size was obviously approximated by finite thickness—large enough to cause no change in the results (2 mm). Since the hemisphere and the half-space are both axi-symmetric, this plane-stress approximation is only a slight simplification of the real case—analogue to the 2D projections of a more realistic 3D model. Later, if needed, we will expand the model to three-dimensional.

The diameter of the hemisphere is 0.4 mm. The infinite half-space is approximated by a large enough finite size (one order of magnitude greater than the size of the bump, namely 4 mm c 2 mm), with zero deformation at the bottom and free edges at the sides. Note that the absolute size of the system is not crucial, only relative distances are important.

The indentation is a flat and rigid object, touching the top of the bump with infinite friction. The high surface-curvature at the junction between the half-space and the hemisphere is effectively reduced with an additional element (linear, inclined at  $45^\circ$ ) to avoid high local stress and error. The hemisphere is approximated with linear elements.

In the model we used two independent loads, both applied with the same perfectly rigid object. One acts purely in the  $x$ , the other in the  $z$ -direction. We assume that deformations are small,

thus in a general case the final deformation can be calculated from the superposition of the two basic indentation types. A general deformation profile caused by an indentation of  $50 \mu\text{m}$  in the two directions can be seen in Fig. 10.

The 3D sensor is positioned at a given depth at  $x=0$ . Note that along the line  $x=0$  in the presented cross-section, neither the  $z$  nor the  $x$ -directional load causes deformation in the other direction (see the vertical lines at the center of Fig. 10b and c). Therefore, if we position our 3D sensor at a given depth along  $x=0$ , the response to the two directions will remain independent.

For determining the proper depth of the sensor we need to take a look at the deformation values along  $x=0$  (Fig. 11), and consider that a minimal thickness of  $200 \mu\text{m}$  is needed below the bump for applicability reasons. Obviously, the thicker the rubber, the more we lose from the sensor's sensitivity for both loading types. As a result, in the experiments the minimal  $200 \mu\text{m}$  thin layer is used.

The last thing needed is the characteristics of the response as a function of the load (Fig. 12).

As can be seen in Fig. 12, up to a deformation of  $100 \mu\text{m}$  – which is quite a high value – all characteristics are close to linear. The response to a normal load is steeper, therefore, the overall normal-to-shear sensitivity of the sensor will differ from one (it is about two now). Since the curves  $FxUz$  and  $FzUx$  are constant zero, the  $x$  and  $z$  components will remain independent, with no cross-talk. Note that our sensors measure the strain, not the deformation. However, characteristics of the strain distribution are similar, thus these results

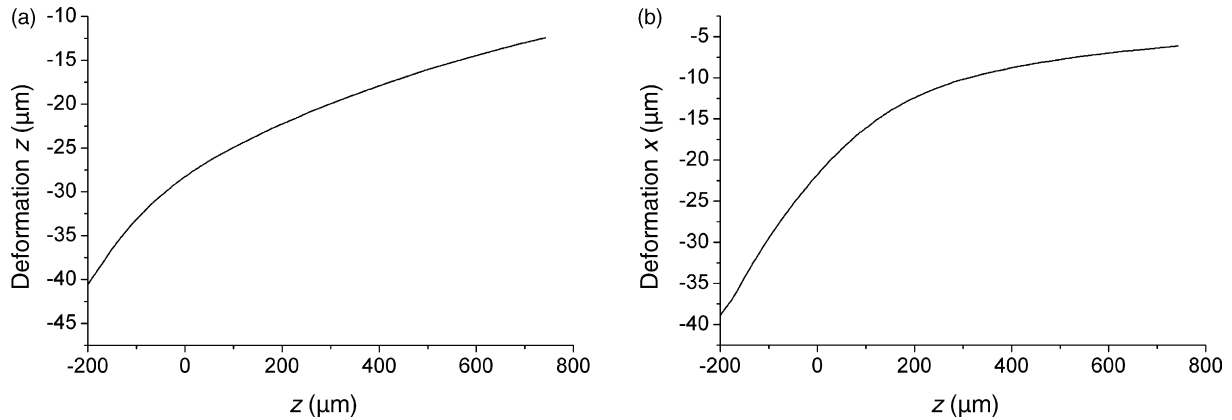


Fig. 11. Deformation values along the axis perpendicular to the surface ( $x=0$ ), at an indentation of  $50\ \mu\text{m}$ . (a) Load:  $z$ , deformation:  $z$ ; (b) load:  $x$ , deformation:  $x$ .

can be used efficiently to predict the functionality of the sensors.

### 6. Texture classification example using the bumpy cover

In this last section we once again use our three-axial MEMS sensors and restrict ourselves to the analysis of the signal of one single taxel, as in the previous sections. The array properties of the same sensors are also investigated in Ref. [16] during a robotic manipulation task. There one smooth object was held between two fingers of a robot arm. Both fingers were equipped with one  $2 \times 2$  sensor array. The continuous signal of the two shear components of each taxel in the  $2 \times 2$  arrays was reduced to the binary direction (+ or -), still resulting in  $2^{8 \times 2} = 65,536$  possible classifiable tactile events, used for tactile feedback for the robot arm. If we enlarge the number of taxels in the array even more, use more than one bit signals and investigate the spatial-temporal response of complex object profiles (as in any of our own general biological tactile-manipulation tasks), any analysis of these complex, multi-dimensional signal arrays will demand high-speed, possibly parallel processing. One ideal cellular-wave-computer for this task is the CNN universal machine [17] that could be our signal-processing hard-

ware in the future on more extended tactile arrays and tasks. Up to now, we have only  $2 \times 2$  sized arrays, but as we said we restrict ourselves even more and first we take a look at the spatial-temporal multi-bit signal of *one single taxel* on textured objects.

To show the functionality of the sensors now equipped with the newly designed bumpy cover, we measure the response of different material types pulled over the hemispheres, and extract simple features from the spatial-temporal signals for a basic texture classification.

We created the described elastic cover again from Elastosil® RT-601, which is a commercially available silicon rubber, with properties described in the previous section. The diameter of the bumps is  $400\ \mu\text{m}$ , as in the finite-element model. The mould for the rubber was made by a silicon wafer. The negative bumps were constructed with simple isotropic etching. Our 3D sensors are arranged in a  $2 \times 2$  array hence four bumps were created with the mould (Fig. 13). The taxel-to-taxel distance in the  $2 \times 2$  MEMS array is  $1.5\ \text{mm}$ .

For the first basic experiments four materials were selected with different texture and roughness. They were pulled over the bumps in all directions, many times within a relatively narrow speed range, but with different amplitude. The characteristic three-axial response to these four materials measured by one of the taxels is shown in Fig. 14.

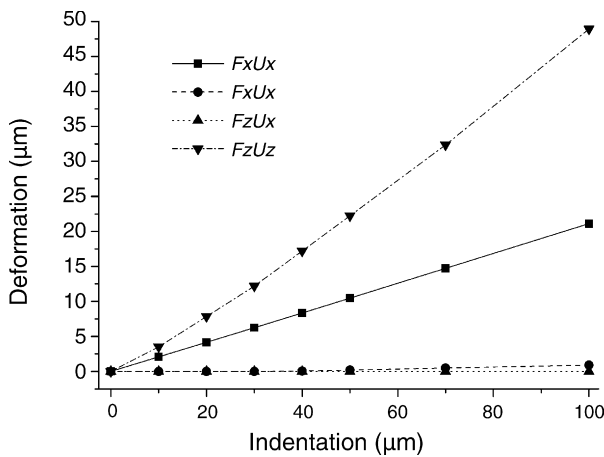


Fig. 12. Deformation values at the 3D sensor location ( $x=0$ ;  $z=200\ \mu\text{m}$ ) as a function of indentation amplitude.  $F_i U_j$  represents the deformation component  $j$  under a load in the  $i$  direction ( $i=x, z$ ;  $j=x, z$ ).

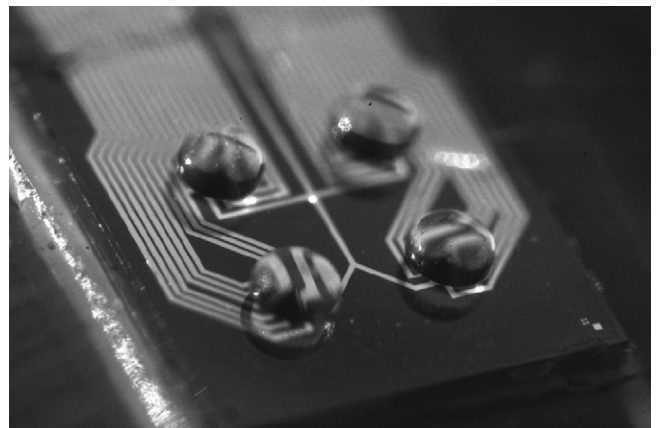


Fig. 13. The  $2 \times 2$  MEMS array with four elastic hemispheres on the interface cover. The distance of the bumps is  $1.5\ \text{mm}$ .

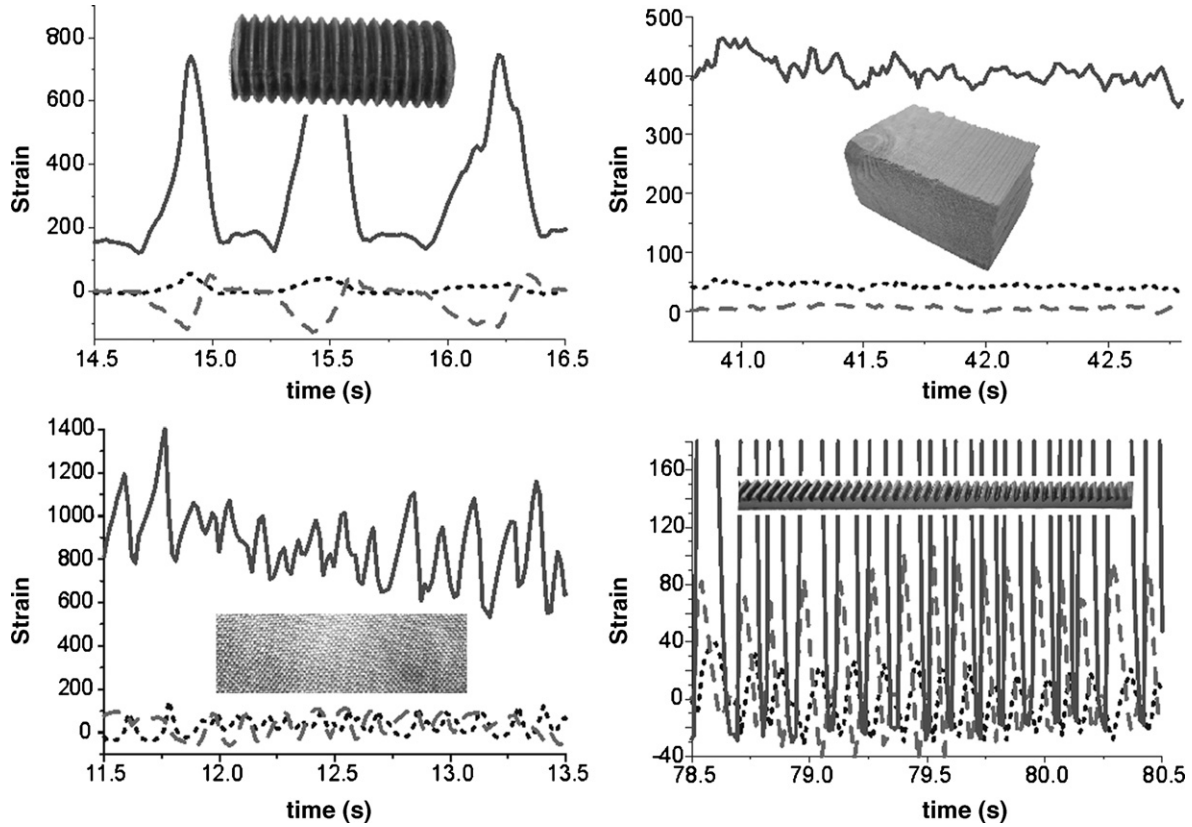


Fig. 14. Characteristic three-axial response of a taxel with a bump to four different materials pulled over the surface in a straight line. The solid line is the normal, the dotted ones are the two shear components. The four materials: screw, smooth wood, fine textile, and rasp.

As can be seen in Fig. 14, the three-axial response of the taxel represents the one-dimensional texture of the materials with characteristic features. The changes in the normal component correspond to the fine structure of the surface, while its averaged amplitude shows how much the object was pressed against the sensor. Motion direction can be extracted from the ratio of the shear components, while the ratio of the shear and normal components determines the friction coefficient. The overall raggedness of the signals corresponds to the surface roughness, etc.

Our aim in the first run was to extract a few simple features from these signals that are available only in three-axial measurements and are insensitive to motion direction and the overall force applied. We selected two features to create a sample two-dimensional classification. One is the *friction coefficient*, averaged on the last  $T$  discrete measurement points at time  $t$ :

$$\bar{\mu}(t) = \sum_{i=t-T}^t \mu(i) = \sum_{i=t-T}^t \sqrt{\frac{T_x(i)^2 + T_y(i)^2}{S_n(i)^2}}. \quad (19)$$

The other one is an arbitrarily chosen, but good descriptive factor of the *surface roughness* that is defined as the normalized standard deviation of the instantaneous friction coefficient, calculated again on  $T$  values:

$$R(t) = \frac{100}{\bar{\mu}(t)} \sqrt{\frac{\sum_{i=t-T}^t (\bar{\mu}(t) - \mu(i))^2}{T-1}}. \quad (20)$$

In the definition of  $R(t)$  the multiplicative factor of 100 is used to push the values of the parameter into the integer range. In the experiments  $T$  was set to 128. Since the scanning time between the frames was 15 ms, the averages at a time were taken from the preceding 2 s, accordingly. The result of the classification on these two parameters, with around 3000 data points can be seen in Fig. 15.

Figs. 14 and 15 show that the three-axial signals coded with the elastic hemispheres represent the object's texture properties with high fidelity, and even our two extracted features give us

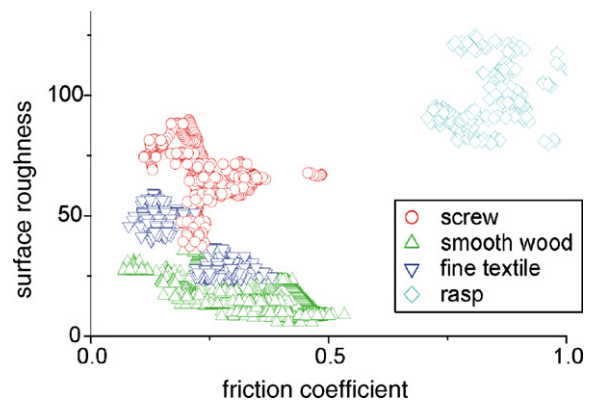


Fig. 15. Result of the first basic texture classification. Each of the approximately 3000 points represents one measurement of the two properties. Although the standard deviation of the properties of each material is huge, the classification is applicable even in this case.

a relatively separable parameter space for texture classification. Introducing some more newly defined characteristic features, the parameter space can be extended to a lot more dimensions and hence the classification can be improved essentially. Nevertheless, this classification is only an example of the many uses of the new three-axial signals. They can be used in many other fields concerning tactile manipulation, texture identification, robotic grip tasks or medical applications, where shear information can improve the quality of the data gained from the tactile-sensors.

## 7. Conclusions

In this paper the effects of the elastic cover on three-axial tactile-sensors were investigated in order to enhance the tactile-event detection capabilities of the overall sensor structure. The cover can be treated as the first spatial–temporal signal-processing layer in tactile tasks—in that framework we investigated how we can benefit from the geometrical design of the elastic layer.

On a *flat* cover we solved the inverse problem of the continuum-mechanical model of the rubber, namely, we gave an analytical solution for reconstructing the location and the amplitude of an arbitrary point load over the surface of the elastic cover of the tactile-sensor. Although there are many a priori simplifying assumptions in the model, experimental qualifications prove its feasibility. Using only one taxel we were able to achieve a kind of tactile hyper-accuracy—we reconstructed the location of a normal, point-like load with around 3  $\mu\text{m}$  accuracy over an area of 300  $\mu\text{m} \times 300 \mu\text{m}$ , with reliable amplitude values, too. Without experimental validation we gave the inverse solution to 3D point-loads, too, and we could also use the same continuum-mechanical framework to calibrate our sensors and determine their normal-to-shear sensitivities.

Proceeding to more complex indentation profiles we broke with the attempt for an analytical inverse-solution, instead we changed our cover geometry from flat to bumpy. With a finite-element model we investigated the information-coding behavior of *elastic hemispheres* on the cover surface. We found that they code normal- and shear-load components independently, with linear behavior, abolishing the need for a complex inverse-solution. In addition, they concentrate the spatial load above the sensors, thereby enhancing the overall functionality and grip of the sensory structure.

In the future we are about to extend our investigations from the analysis of one taxel to a tactile array, using a cellular-wave-computer for signal-processing and our new 8  $\times$  8 element, three-axial tactile-sensor array.

## Acknowledgments

Special thanks are due to the Research Institute for Technical Physics and Materials Science (MFA) of the Hungarian Academy of Sciences for creating the 3D sensors. This work was partly supported by the Hungarian Scientific Research Fund (OTKA) via grant no. TS040858 and the “Telesense Project” of the National R&D Program (NKFP 2001/2/035). Discus-

sions with Ferenc Kovács, Péter Szolgay and Attila Kis are also gratefully acknowledged.

## References

- [1] J.R. Phillips, K.O. Johnson, Tactile spatial resolution. III. A continuum mechanics model of skin predicting mechanoreceptor responses to bars, edges, and gratings, *J. Neurophysiol.* 46 (6) (1981) 1204–1225.
- [2] K.L. Johnson, *Contact Mechanics*, Cambridge University Press, 1985.
- [3] R.S. Fearing, J.M. Hollerbach, Basic solid mechanics for tactile sensing, *Int. J. Robot. Res.* 4 (3) (1985) (Fall).
- [4] R.S. Fearing, Tactile sensing mechanisms, *Int. J. Robot. Res.* 9 (3) (1990) 3–23.
- [5] R.S. Fearing, T.O. Binford, Using a cylindrical tactile-sensor for determining curvature, *IEEE Trans. Robot. Automat.* 7 (6) (1991) 806–817.
- [6] A. Caiti, G. Canepa, D. De Rossi, F. Germagnoli, G. Magenes, T. Parisini, Towards the realization of an artificial tactile system: fine-form discrimination by a tensorial tactile-sensor array and neural inversion algorithms, *IEEE Trans. Syst. Man Cybern.* 25 (6) (1995) 933–946.
- [7] N. Chen, H. Zhang, R. Rink, Tactile sensing of point contact, in: *IEEE International Conference on Systems, Man and Cybernetics, 1995. 'Intelligent Systems for the 21st Century'*, vol. 1, 22–25 October, 1995, pp. 574–579.
- [8] S.J. Bolanowski, L. Pawson, Organization of Meissner corpuscles in the glabrous skin of monkey and cat, *Somatosens. Mot. Res.* 20 (3–4) (2003) 223–231.
- [9] G.J. Gerling, G.W. Thomas, The Effect of Fingertip Microstructures on Tactile Edge Perception, *WHC*, 2005, pp. 63–72.
- [10] T. Maeno, K. Kobayashi, N. Yamazaki, Relationship between the structure of human finger tissue and the location of tactile receptors, *JSME Int. J.* 41 (1998) 94–100.
- [11] D. Yamada, T. Maeno, Y. Yamada, Artificial finger skin having ridges and distributed tactile-sensors used for grasp force control, *J. Robot. Mechatron.* 14 (2) (2002) 140–146.
- [12] M.R. Tremblay, M.R. Cutkosky, Estimating friction using incipient slip sensing during a manipulation task, in: *Proceedings of the 1993 IEEE International Conference on Robotics and Automation, 1993*, pp. 429–434.
- [13] G. Vásárhelyi, M. Ádám, É. Vázsonyi, Zs. Vízváry, A. Kis, I. Bársony, Cs. Dücső, Characterization of an integrable single-crystalline 3D tactile-sensor, *IEEE Sens. J.* 6 (4) (2006) 928–934.
- [14] G. Vásárhelyi, M. Ádám, É. Vázsonyi, I. Bársony, Cs. Dücső, Effects of the elastic cover on tactile-sensor arrays, *Sens. Actuators A: Phys.* 132 (2006) 245–251.
- [15] É. Vázsonyi, M. Ádám, Cs. Dücső, Zs. Vízváry, A.L. Tóth, I. Bársony, Three-dimensional force sensor by novel alkaline etching technique, *Sens. Actuators A: Phys.* 123–124 (23) (2005) 620–626.
- [16] A. Kis, F. Kovács, P. Szolgay, 3D tactile-sensor array processed by CNN-UM: a fast method for detecting and identifying slippage and twisting motion, *Int. J. Circuit Theor. Application (CTA)* 34 (2006) 517–531 (special issue on CNN).
- [17] T. Roska, L.O. Chua, The CNN universal machine: an analogic array computer, *IEEE Trans. Circuit Syst. II* 40 (1993) 163–173.

## Biographies

**Gábor Vásárhelyi** was born in Budapest, Hungary, in 1979. He received his MSc degree in engineering-physics from the Technical University of Budapest, Hungary, in 2003. He is currently a PhD student at Péter Pázmány Catholic University, Multidisciplinary Technical Sciences Doctoral School, Budapest, Hungary. Main research fields are tactile-sensor arrays and tactile applications on CNN chips.

**Balázs Fodor** was born in Csorna, Hungary, in 1985. He is currently a student at the Hungarian Technical University of Budapest (he is in his fourth year). Main research fields are FEM analysis of composite structures and nonlinear FEM analysis.

**Tamás Roska** was born in Hungary in 1940. He received his MSc degree in electrical engineering from the Technical University of Budapest, Hungary, in 1964 and the PhD and DSc degrees in 1973 and 1982, respectively. From 1964 to 1970, he was with the Measuring Instrument Research Institute, Budapest, Hungary. From 1970 to 1982, he was with the Research Institute for Telecommunication, Budapest, Hungary. Since 1982, he has been with the Computer and Automation Institute, Hungarian Academy of Sciences, where he is Head of the Analogic and Neural Computing Research Laboratory. Since 1989, he has been a visiting scholar at the Department of Electrical Engineering and Computer Sciences and the Electronics Research Laboratory each year and was recently a visiting research professor at the Vision Research Laboratory of the University of California at Berkeley. He is also the founder Dean of the Faculty of Information Technology at Péter Pázmány Catholic University, Budapest. His main

research areas are cellular neural networks, nonlinear circuits and systems, and analogic spatiotemporal supercomputing. Dr. Roska has been a member of the Technical Committee on Nonlinear Circuits and Systems of the IEEE Circuits and Systems Society since 1975. Recently, he has served twice as Associate Editor of the IEEE Transactions on Circuits and Systems, and later as Editor-in-Chief of the IEEE Transactions on Circuits and Systems. I: Fundamental Theory and Applications. He received the IEEE Fellow Award for contributions to the qualitative theory of nonlinear circuits and the theory and design of programmable cellular neural networks. In 1993, he was elected a Member of the Academia Europaea (European Academy of Sciences, London) and the Hungarian Academy of Sciences. In 1999, he became the Founding Chair of the Technical Committee on Cellular Neural Networks and Array Computing of the IEEE Circuits and Systems Society.